Preprints (www.preprints.org) | NOT PEER-REVIEWED | Posted: 9 February 2018 doi:10.20944/preprints201802.0078.v1

Peer-reviewed version available at Energies 2018, 11, 724; doi:10.3390/en11040724

Exploring the Potential of Camber Control to Improve Vehicles' Energy Efficiency during Cornering

Peikun Sun[a*], Annika Stensson Trigell[a], Lars Drugge[a], Jenny Jerrelind[a], Mats Jonasson[a,b]

[a]*KTH Vehicle Dynamics, Department of Aeronautical and Vehicle Engineering, KTH Royal Institute of Technology, Teknikringen 8, SE-100 44 Stockholm, Sweden; peikun@kth.se (P.S.); annika@kth.se (A.S.T.); larsd@kth.se (L.D.); jennyj@kth.se (J.D.); mats.jonasson@volvocars.com (M.J.)*

[b]*Volvo Cars, SE-405 31 Gothenburg, Sweden.*

[Abstract] Actively controlling the camber angle to improve energy efficiency has recently gained interest due to the importance of reducing energy consumption and the driveline electrification trend that makes cost-efficient implementation of actuators possible. To analyse how much energy that can be saved with camber control, the effect of changing the camber angles on the forces and moments of the tyre under different driving conditions should be considered. In this paper, Magic Formula tyre models for combined slip and camber are used for simulation of energy analysis. The components of power loss during cornering are formulated and used to explain the influence that camber angles have on the power loss. For the studied driving paths and the assumed driver model, the simulation results show that active camber control can have considerable influence on power loss during cornering. Different combinations of camber angles are simulated, and a camber control algorithm is proposed and verified in simulation. The results show that the camber controller has very promising application prospects for energy-efficient cornering.

[Keywords] Energy saving, cornering, camber, Magic Formula

1. Introduction

As concern for environmental pollution and climate change grows, new energy-efficient vehicles, in particular electric vehicles, have gained more and more attention. Electrified powertrains make decentralized driving systems possible, among which the in-wheel motors (IWM) are one important technology [1]. Electric vehicles with four in-wheel motors (4IWM) can directly and independently control their four wheels and can realise more advanced motion control than other types of vehicles. Besides better vehicle performance and safety control, energy-efficient control can also be carried out at the same time, and has been considered a very important field of research since energy-efficient electric vehicles can improve their popularity.

There are several studies about direct yaw moment control (DYC) for the improvement of vehicle handling and stability [2,3]. A 4IWM electric vehicle can easily implement DYC and the contribution of DYC to energy saving during cornering has been studied [4,5], but its contribution is normally limited. Other researchers are studying optimal torque distribution to improve energy efficiency [6,7], where the studies are usually conducted by incorporating the IWM efficiency map.

Electrification of vehicle actuators such as steering actuators and camber actuators provides opportunities for more advanced suspension designs, i.e. the active wheel corner

© 2018 by the author(s). Distributed under a Creative Commons CC BY license.

Preprints (www.preprints.org) | NOT PEER-REVIEWED | Posted: 9 February 2018 doi:10.20944/preprints201802.0078.v1

Peer-reviewed version available at Energies 2018, 11, 724; doi:10.3390/en11040724

module (ACM) [8], shown in Figure 1. In addition to 4IWMs, ACM can also realise individual wheel steering and active tyre camber control. In conventional vehicles, tyre camber angles are usually passively tilted according to suspension geometry that limits the possible ranges. Electric vehicles with ACM suspension design can have up to 12 control variables: 4 wheel drives, 4 steering controls and 4 camber controls. This is realised in the research concept vehicle with wheel corner module functionality, developed by KTH Royal Institute of Technology and shown in Figure 2.

Publications about controlling the camber angles to reduce energy consumption are quite few. There are some examples of research combining DYC with active camber control [9,10] and its effects on energy saving have also been studied [11,12]. From the results, the percentage of energy reduction seems promising. However, only camber's effect on the lateral force was considered and no applicable camber controller has been suggested.

The aim of this work is to analyse how the camber affects power loss during cornering. The components of power loss, which includes the power to control camber angles are established. The longitudinal and lateral tyre forces interact with each other, especially in the case of high lateral acceleration during which the slip angle can be large enough to greatly influence the longitudinal forces. In addition, the camber angle could also cause changes to the forces and moments of the tyre [13-15]. For this reason, Magic Formula tyre models for longitudinal force, lateral force, overturning moment and aligning moment are adopted for simulation. Furthermore, a driver model and a method for camber control are designed to follow the designed paths. Two paths and three combinations of camber controls are chosen to primarily study camber's effect on the components of power loss. After that, more comprehensive simulation settings are then studied and an applicable camber controller is proposed and verified by simulation.

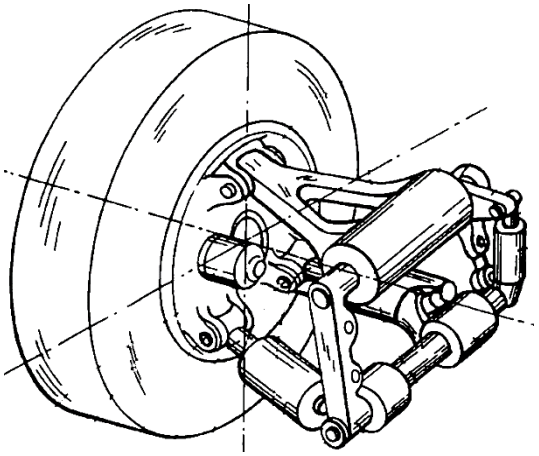

Figure 1. Active wheel corner module [8].

Figure 2. KTH Research concept vehicle.

2. Power loss during cornering

When a tyre travels with a camber angle, the component of rolling resistance moment on rolling resistance will be reduced and a component of aligning moment on rolling resistance will appear [16,17]. In this study, the kinetic equation describing the tyre taking into account the effects of camber angle is introduced. A two-track vehicle model is applied to derive the

Preprints (www.preprints.org) | NOT PEER-REVIEWED | Posted: 9 February 2018 doi:10.20944/preprints201802.0078.v1

Peer-reviewed version available at Energies 2018, 11, 724; doi:10.3390/en11040724

power loss during cornering, and the power needed to control the camber angles is estimated.

2.1 Tyre kinetics with camber control

From Figure 3, the equation of motion in the longitudinal direction without camber control can be written as

$$T - M_y - F_x R_0 = I_w \dot{\omega} \tag{1}$$

where T is the driving moment, M_y is the rolling resistance moment, F_x is the longitudinal force of the tyre, R_0 is the effective radius of the tyre, I_w is the wheel rotational inertia and ω is wheel angular velocity.

In Figure 4, the effect of camber is taken into account. While keeping the same camber angle during driving, the direction of T is perpendicular to the wheel plane. The equation of motion can then be written as

$$T - M_y \cos\gamma - M_z \sin\gamma - F_x R_0 = I_w \dot{\omega} \tag{2}$$

where M_z is the aligning moment and γ is the camber angle.

The rolling resistance moment M_y can be expressed as

$$M_y = f_{rr} \cdot F_z \cdot R_0 \tag{3}$$

where F_z is the vertical force of the tyre and f_{rr} is the rolling resistance coefficient.

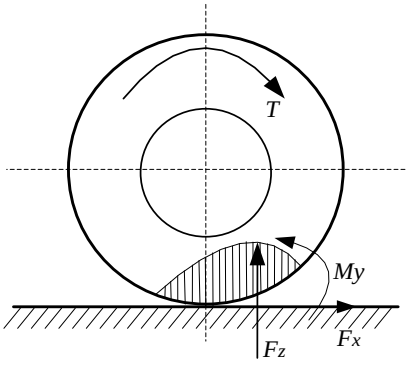

Figure 3. Tyre without camber angle.

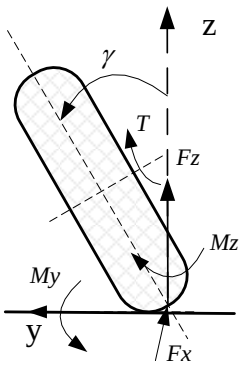

Figure 4. Tyre with camber angle.

2.2 The power for propulsion of the wheels

As shown in Figure 5, a two-track vehicle model is formulated and front wheel steering is adopted. The longitudinal, lateral and yaw motions are formulated in Equations (4) to (6)

$$m \cdot a_x = F_{x1}\cos\delta_f + F_{x2}\cos\delta_f + F_{x3} + F_{x4} - F_{y1}\sin\delta_f - F_{y2}\sin\delta_f - F_{ar} \tag{4}$$

$$m \cdot a_y = F_{x1}\sin\delta_f + F_{y1}\cos\delta_f + F_{x2}\sin\delta_f + F_{y2}\cos\delta_f + F_{y3} + F_{y4} \tag{5}$$

Preprints (www.preprints.org) | NOT PEER-REVIEWED | Posted: 9 February 2018 doi:10.20944/preprints201802.0078.v1

Peer-reviewed version available at Energies 2018, 11, 724; doi:10.3390/en11040724

$$I_z \cdot \ddot{\psi} = \left(F_{x1}\sin\delta_f + F_{y1}\cos\delta_f + F_{x2}\sin\delta_f + F_{y2}\cos\delta_f\right)l_f - \left(F_{y3} + F_{y4}\right)l_r + \left(F_{x2}\cos\delta_f - F_{y2}\sin\delta_f - F_{x1}\cos\delta_f + F_{y1}\sin\delta_f + F_{x4} - F_{x3}\right)\frac{t_w}{2} \quad (6)$$

where, m is the vehicle mass, a_x is the longitudinal acceleration ($a_x = \dot{V}_x - V_y\dot{\psi}$), a_y is the lateral acceleration ($a_y = \dot{V}_y + V_x\dot{\psi}$), V_x is the forward speed, V_y is the lateral speed, ψ is the yaw angle, F_{x1}, F_{x2}, F_{x3} and F_{x4} are longitudinal forces at each tyre respectively, F_{y1}, F_{y2}, F_{y3} and F_{y4} are lateral forces at each wheel respectively, F_{ar} is the aerodynamic resistance, δ_f is the steering angles for the front wheels, I_z is the moment of yaw inertia, l_f is the distance from centre of gravity (CoG) to front axle, l_r is the distance from CoG to rear axle, and t_w is wheel track width (the subscript, 1: front left; 2: front right; 3: rear left; 4: rear right). The steering angle is assumed to be small ($\sin\delta_f \approx \delta_f$, $\cos\delta_f \approx 1$).

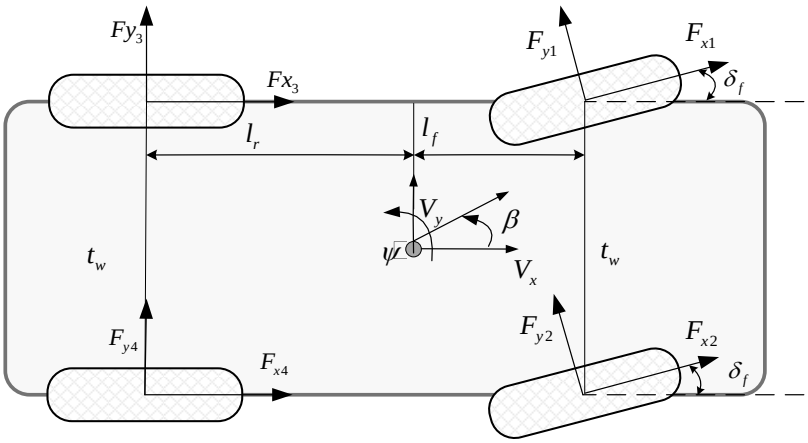

Figure 5. Two-track vehicle model.

Slip angles (α_1, α_2, α_3 and α_4) for each wheel are expressed as

$$\alpha_1 = \frac{V_y + \dot{\psi}l_f}{V_x - \frac{t_w}{2}\dot{\psi}} - \delta_f;\ \alpha_2 = \frac{V_y + \dot{\psi}l_f}{V_x + \frac{t_w}{2}\dot{\psi}} - \delta_f;\ \alpha_3 = \frac{V_y - \dot{\psi}l_r}{V_x - \frac{t_w}{2}\dot{\psi}};\ \alpha_4 = \frac{V_y - \dot{\psi}l_r}{V_x + \frac{t_w}{2}\dot{\psi}}; \quad (7)$$

The angular velocity of the i_{th} wheel can be expressed as

$$\omega_i = \frac{(1+\kappa_i)V_i}{R_0} \quad (8)$$

where κ_i is the slip ratio and V_i is the forward speed of the i_{th} wheel. The equations for forward speed for each individual wheel can be expressed as

$$V_1 = V_x - \frac{t_w}{2}\dot{\psi};\ V_2 = V_x + \frac{t_w}{2}\dot{\psi};\ V_3 = V_x - \frac{t_w}{2}\dot{\psi};\ V_4 = V_x + \frac{t_w}{2}\dot{\psi}; \quad (9)$$

Preprints (www.preprints.org) | NOT PEER-REVIEWED | Posted: 9 February 2018 doi:10.20944/preprints201802.0078.v1

Peer-reviewed version available at Energies 2018, 11, 724; doi:10.3390/en11040724

The power for the propulsion of the wheels P_w can be derived from the sum of the product of the driving moment and angular velocity of each wheel,

$$P_w = \sum_{i=1}^{4} T_i \cdot \omega_i \tag{10}$$

Re-writing Equation (2) for each wheel

$$T_i - M_{yi}\cos\gamma_i - M_{zi}\sin\gamma_i - F_{xi}R_0 = I_w\dot{\omega}_i \tag{11}$$

By substituting Equations (4)-(9) as well as Equation (11) into Equation (10) makes it possible to reformulate P_w as

$$\begin{aligned} P_w = {} & F_{ar}V_x + \sum_{i=1}^{4}\left(M_{yi}\cos\gamma_i + M_{zi}\sin\gamma_i\right)\omega_i + \sum_{i=1}^{4}F_{xi}\kappa_i V_i + \sum_{i=1}^{4}\left(-F_{yi}\alpha_i\right)V_x \\ & + m\dot{V}_x V_x + \sum_{i=1}^{4} I_w\dot{\omega}_i\omega_i + I_z\dot{\psi}\ddot{\psi} + m\dot{V}_y V_y + P_a \end{aligned} \tag{12}$$

$$P_a = \left(F_{y1}\alpha_1 - F_{y2}\alpha_2 + F_{y3}\alpha_3 - F_{y4}\alpha_4\right)\left(\frac{t_w}{2}\dot{\psi}\right) - \left(F_{x1}\delta_f + F_{x2}\delta_f\right)\left(V_y + l_f\dot{\psi}\right) \tag{13}$$

where $F_{ar}V_x$ is aerodynamic loss, $\sum_{i=1}^{4}\left(M_{yi}\cos\gamma_i + M_{zi}\sin\gamma_i\right)\omega_i$ is rolling resistance loss, $\sum_{i=1}^{4}F_{xi}\kappa_i V_i$ is longitudinal slip loss, $\sum_{i=1}^{4}\left(-F_{yi}\alpha_i\right)V_x$ is lateral slip loss, $m\dot{V}_x V_x$ is longitudinal acceleration loss, $\sum_{i=1}^{4} I_w\dot{\omega}_i\omega_i$ is the wheel angular acceleration loss, $I_z\dot{\psi}\ddot{\psi}$ is yaw acceleration loss, $m\dot{V}_y V_y$ is lateral acceleration loss, and P_a can be classified as additional loss.

For the aerodynamic resistance, F_{ar} can be expressed as:

$$F_{ar} = \frac{1}{2}C_{ar}\rho A V_x^2 \tag{13}$$

where C_{ar} is the coefficient of aerodynamic resistance, ρ is density of the air, and A is frontal area of the vehicle. The vertical forces of each wheel are expressed as:

$$\begin{cases} F_{z1} = m\left(\frac{1}{2}gl_r - \frac{1}{2}a_x h - \frac{l_r}{t_w}a_y h\right)\Big/\left(l_f + l_r\right) \\ F_{z2} = m\left(\frac{1}{2}gl_r - \frac{1}{2}a_x h + \frac{l_r}{t_w}a_y h\right)\Big/\left(l_f + l_r\right) \\ F_{z3} = m\left(\frac{1}{2}gl_f + \frac{1}{2}a_x h - \frac{l_f}{t_w}a_y h\right)\Big/\left(l_f + l_r\right) \\ F_{z4} = m\left(\frac{1}{2}gl_f + \frac{1}{2}a_x h + \frac{l_f}{t_w}a_y h\right)\Big/\left(l_f + l_r\right) \end{cases} \tag{14}$$

where h is the height of CoG and g is the acceleration of gravity (g=9.8 m/s^2).

Preprints (www.preprints.org) | NOT PEER-REVIEWED | Posted: 9 February 2018 doi:10.20944/preprints201802.0078.v1

Peer-reviewed version available at Energies 2018, 11, 724; doi:10.3390/en11040724

2.3 The power for controlling camber angles

The power that is needed to control the camber angle for each tyre can be calculated by multiplying the overturning moment M_{xi} by the time derivative of the camber angle $\dot{\gamma}_i$. It is not considered when $M_{xi}\dot{\gamma}_i < 0$. The estimated total power for controlling the camber angle of all four tyres is then ,

$$P_{camber} = \sum_{i=1}^{4} M_{xi}\dot{\gamma}_i \quad (M_{xi}\dot{\gamma}_i \geq 0,\ i = 1,2,3,4) \tag{15}$$

The power loss during cornering P_{all} is the sum of P_w and P_{camber} i.e.,

$$P_{all} = P_w + P_{camber} \tag{16}$$

3. Tyre model

In this paper, Magic Formula tyre models for longitudinal force, lateral force, overturning moment and aligning moment under combined-slip and camber are used. Magic Formula is a semi-empirical equation that can closely match the experimental data [15]. The equations are as follows:

$$F_x = G_{x\alpha}\left(D_x \sin\left[C_x \arctan\left\{B_x\left(\kappa + S_{Hx}\right) - E_x\left(B_x\left(\kappa + S_{Hx}\right) - \arctan\left(B_x\left(\kappa + S_{Hx}\right)\right)\right)\right\}\right] + S_{Vx}\right) \tag{17}$$

$$F_y = G_{y\kappa}\left(D_y \sin\left[C_y \arctan\left\{B_y\left(\alpha + S_{Hy}\right) - E_y\left(B_y\left(\alpha + S_{Hy}\right) - \arctan\left(B_y\left(\alpha + S_{Hy}\right)\right)\right)\right\}\right] + S_{Vy}\right) + S_{Vy\kappa} \tag{18}$$

$$M_x = F_z R_0\left(q_{sx1} - q_{sx2}\gamma + q_{sx3} F_y / F_{z0}\right) \tag{19}$$

$$M_z = M_{zr} - t\cdot\left(F_y - S_{Vy\kappa}\right) + s\cdot F_x \tag{20}$$

where $G_{y\alpha}$ and $G_{y\kappa}$ are weighting factors, S_{Hx} is the horizontal shift for κ, which is dependent on the vertical load, S_{Hy} is the horizontal shift for α, which is a function of vertical load and camber angle, $B_x, C_x, D_x\ E_x\ B_y, C_y, D_y$ and E_y are curve factors, q_{sx1}, q_{sx2} and q_{sx3} are coefficients for M_x, F_{z0} is the nominal vertical force, $S_{Vy\kappa}$ is referred to the κ-induced ply-steer, M_{zr} is the residual torque, t is pneumatic trail, s is the moment arm which arises for F_x as a result of camber angle γ and lateral tyre deflection due to F_y (the specific coefficients can be referred to in Appendix 3 of [15]). Examples of F_x, F_y, M_x and M_z under combined-slip conditions and camber are shown in Figure 6.

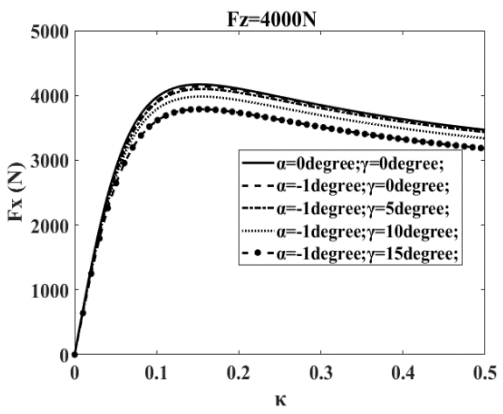

(a) Longitudinal force versus slip ratio.

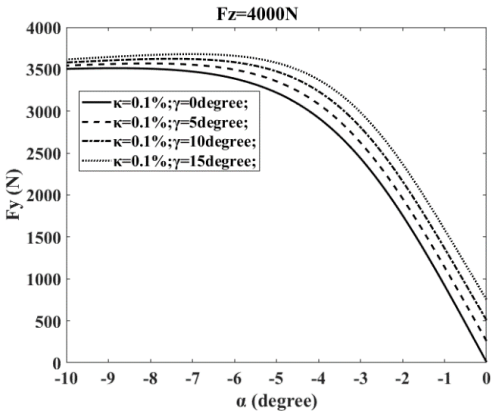

(b) Lateral force versus slip angle.

Preprints (www.preprints.org) | NOT PEER-REVIEWED | Posted: 9 February 2018 doi:10.20944/preprints201802.0078.v1

Peer-reviewed version available at Energies 2018, 11, 724; doi:10.3390/en11040724

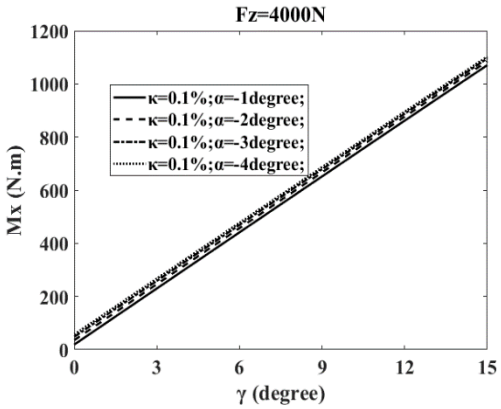

(c) Overturning moment versus camber angle.

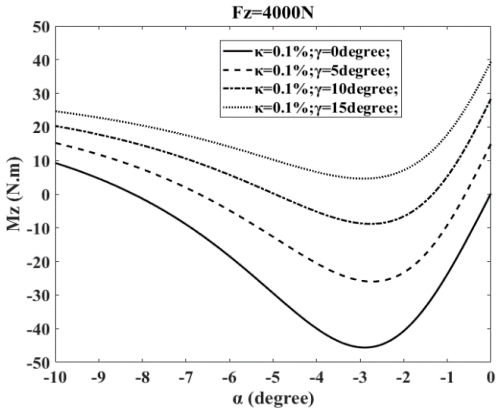

(d) Aligning moment versus slip angle.

Figure 6. Magic Formula tyre characteristics [15].

4. Energy saving with camber control

In order to analyse how much contribution the camber can make to energy saving during cornering, paths are designed and a driver model is developed to follow the path and reference velocity. Then, a method for camber control is proposed and the changes in P_{camber} and the components in Equation (12) are analysed.

4.1 Path design

By analysing the vehicle characteristics in steady-state cornering, the fundamental vehicle motion characteristics can be understood [18]. In steady-state cornering, the power remains constant. However, the dynamic power change during transient cornering when entering or exiting a corner is also important.

The chosen path is shown in Figure 7. The path consists of three parts: two straight lines with length L and a half-circle with radius R. In this paper, the longitudinal acceleration of the vehicle is not considered, namely, $\dot{V}_x = 0$, i.e. the vehicle is assumed to follow the path at constant velocity. The vehicle first runs straight, then gradually reaches steady-state cornering ($\dot{V}_x = 0$, $\dot{V}_y = 0$ and $\ddot{\psi} = 0$) after entering the circle, after which it exits the circle and runs straight again.

4.2 Driver model

The driver model consists of two parts: a speed controller and a steering controller. In this paper, a PID speed controller is designed to follow the reference speed and the torques of the four wheels are assumed to be equal i.e., $T_1=T_2=T_3=T_4$. The steering controller is based on the multiple-preview point steering theory [19-21]. Figure 8 shows a basic schematic diagram of this steering controller. As shown in the figure, the controller has three inputs: the lateral offset Δy_1 between the vehicle and the road at the current position, the yaw angle offset $\Delta\psi$ between the vehicle yaw angle ψ_v and the road heading angle ψ_r and the lateral offset Δy_2 at preview distance l ahead of the vehicle. The l is the product of preview time t_p and the vehicle forward speed V_x, i.e., $l = V_x t_p$. The front steering angle δ_f can be determined as

Preprints (www.preprints.org) | NOT PEER-REVIEWED | Posted: 9 February 2018 doi:10.20944/preprints201802.0078.v1

Peer-reviewed version available at Energies 2018, 11, 724; doi:10.3390/en11040724

$$\delta_f = k_y \Delta y_1 + k_\psi \Delta\psi + k_l \Delta y_2 \tag{21}$$

where k_y, k_ψ and k_l are gains for each input.

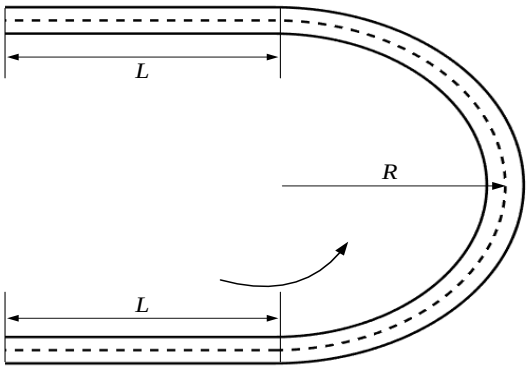

Figure 7. Path design.

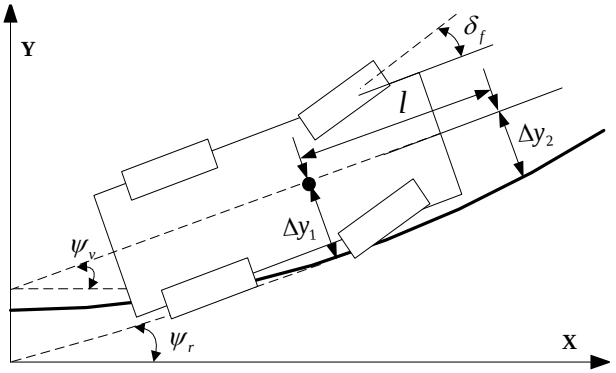

Figure 8. Steering controller.

For the control of camber angle, the range of camber angle is assumed to be $[-15^0, 15^0]$ and for the path in Figure 7 the steering wheel is turned to the left and the range of the steering angle δ_f is $[0, 25^0]$. The camber angles of both front wheels, γ_1 and γ_2, are set to the same value, and so are also the camber angles of both rear wheels, γ_3 and γ_4, i.e., $\gamma_1 = \gamma_2$ and $\gamma_3 = \gamma_4$. For the control of the camber angle, the relationships between camber angles and front steering angle are defined as:

$$\gamma_1 = \gamma_2 = \begin{cases} K_{12}\delta_f & \left|K_{12}\delta_f\right| \le 15^0 \\ sign\left(K_{12}\delta_f\right)\cdot 15^0 & else \end{cases} \tag{22}$$

$$\gamma_3 = \gamma_4 = \begin{cases} K_{34}\delta_f & \left|K_{34}\delta_f\right| \le 15^0 \\ sign\left(K_{34}\delta_f\right)\cdot 15^0 & else \end{cases} \tag{23}$$

where K_{12} and K_{34} are coefficients which determine the relationship between camber and steering angle. When K_{12} or K_{34} is larger than zero, this means that the front or rear wheels are tilted in the same direction as δ_f. Figure 9 gives rear views of the vehicle with camber control with different combinations of K_{12} and K_{34}.

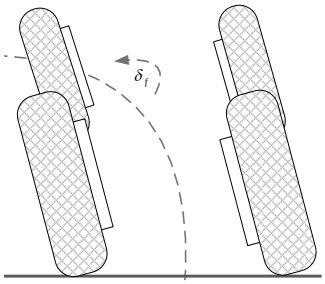

(a) $K_{12}>0$; $K_{34}>0$

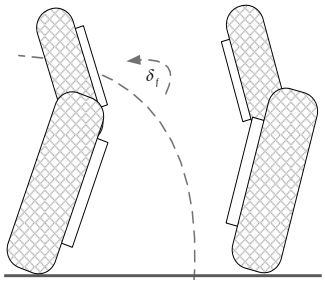

(b) $K_{12}>0$; $K_{34}<0$

Preprints (www.preprints.org) | NOT PEER-REVIEWED | Posted: 9 February 2018 doi:10.20944/preprints201802.0078.v1

Peer-reviewed version available at Energies 2018, 11, 724; doi:10.3390/en11040724

(c) K_{12}<0; K_{34}>0 (d) K_{12}<0; K_{34}<0

Figure 9. Rear views of the vehicle with different settings on camber control coefficient K_{12} and K_{34}.

4.3 Analysis of components of power loss

In order to analyse how the power loss during cornering P_{all} changes, the simulation model is implemented in Matlab and Dymola. The simulation setups presented in Table 2 are used. The path parameters L=60 m and R=100 m are adopted; two lateral accelerations at steady-state cornering 3 m/s^2 and 6 m/s^2 are used and corresponding velocities are calculated; three different combinations of K_{12} and K_{34} are simulated. The P_{all} can be a function of K_{12} and K_{34} under a given path and velocity.

Table 2. Parameters chosen for analysing the components of total power loss.

L (m)	R (m)	V_x (km/h)	a_y (m/s^2)	K_{12}	K_{34}
60	100	62.3	3	0	0
60	100	62.3	3	4	4
60	100	62.3	3	9	9
60	100	88.1	6	0	0
60	100	88.1	6	4	4
60	100	88.1	6	9	9

The vehicle parameters are shown in Table 3 and the density of the air is ρ=1 kg/m^3. In [22], it was shown that the effect of camber on f_{rr} is low, so in this paper it is kept constant and is given a value of $f_{rr} = 0.01$.

Table 3. Vehicle parameters.

Parameters	Values	Parameters	Values
m	1500 kg	I_w	1 kgm^2
I_z	1700 kgm^2	C_{ar}	0.3
l_f	1.2 m	A	2 m^2
l_r	1.5 m	R_0	0.3 m
t_w	1.65 m	h	0.48 m

With the driver model, firstly the vehicle can keep the reference speed; secondly, the vehicle can track the reference path. Since the vehicle has the same speed and the same path with and without camber control, the simulation results can be compared. The aerodynamic loss remains the same at a certain velocity. At 62.3 km/h the aerodynamic loss is 1558 W and at 88.1 km/h 4406 W. The change in steering angle, camber angle, P_{all}, P_{camber}, P_w and the components of P_w are shown in Figures 10 and 11.

If the same camber angles for front and rear tyres are implemented, the front steering angle does not change much from Figure 10(a) to Figure 11(a). The main components of P_w are aerodynamic loss, rolling resistance loss and lateral slip loss. Although controlling camber can cost power, which is shown in Figures 10(d) and 11(d), the total power loss can still be reduced while entering the corner, which is shown in Figure 10(c) K_{12}=K_{34}=4, 9 and Figure

Preprints (www.preprints.org) | NOT PEER-REVIEWED | Posted: 9 February 2018 doi:10.20944/preprints201802.0078.v1

Peer-reviewed version available at Energies 2018, 11, 724; doi:10.3390/en11040724

11(c) K_{12}=K_{34}=4, 9. From Figures 10(g) and 11(g), implementing positive camber control coefficients can greatly reduce lateral slip loss. The reduction of this part of power loss can be explained by studying Figure 6(b). It can be seen that keeping the same lateral force, the camber thrust can reduce the absolute value of slip angle and consequently, the lateral slip loss is reduced.

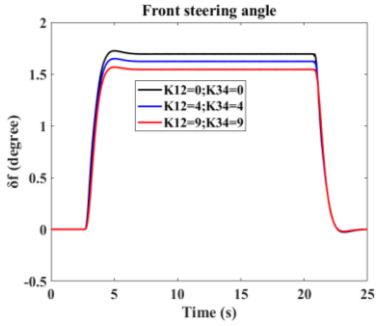

(a) Front steering angle

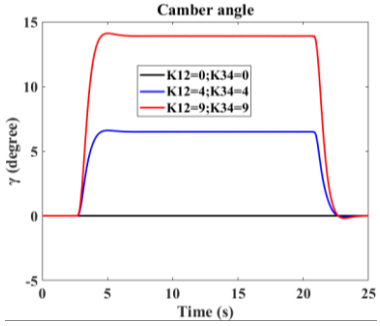

(b) Camber angle

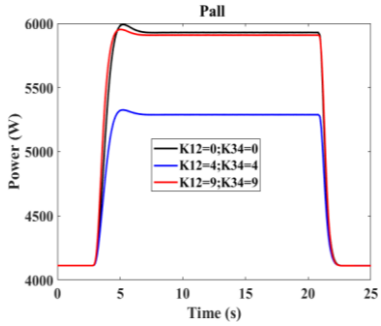

(c) P_{all}

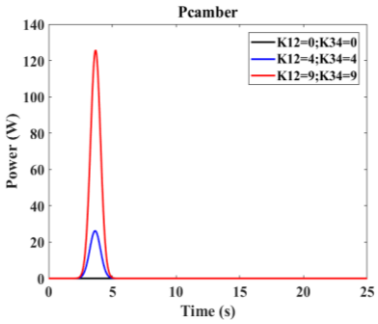

(d) P_{camber}

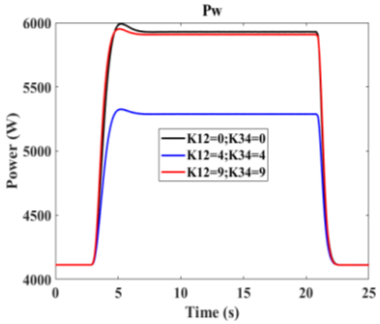

(e) P_w

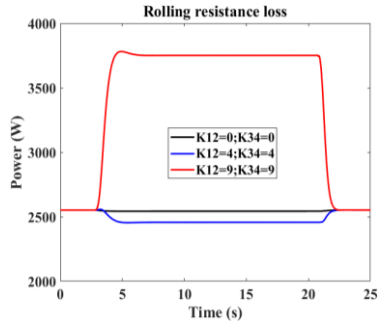

(f) Rolling resistance loss

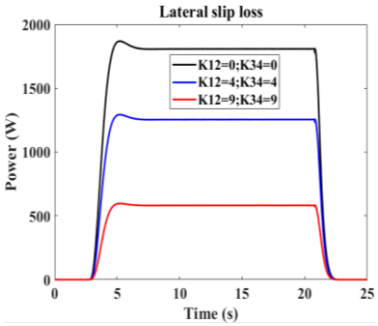

(g) Lateral slip loss

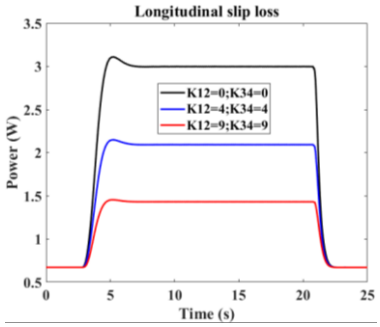

(h) Longitudinal slip loss

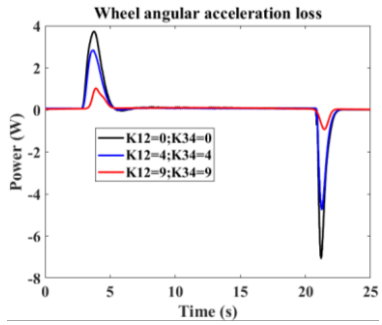

(i) Wheel angular acceleration loss

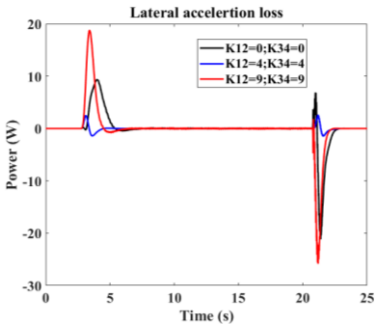

(j) Lateral acceleration loss

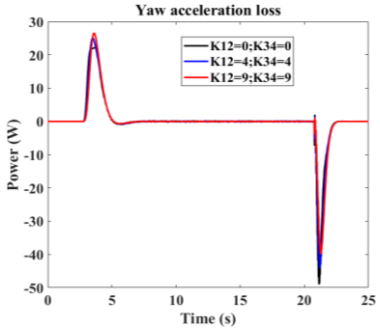

(k) Yaw acceleration loss

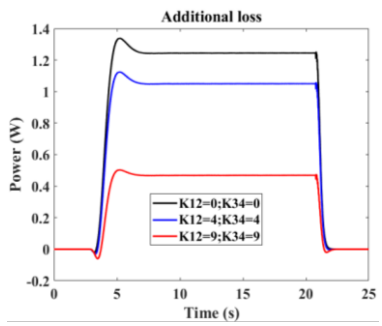

(l) Additional loss

Figure 10. Steering and camber angles as well as power losses at R=100 m and V_x=62.3 km/h.

Preprints (www.preprints.org) | NOT PEER-REVIEWED | Posted: 9 February 2018 doi:10.20944/preprints201802.0078.v1

Peer-reviewed version available at Energies 2018, 11, 724; doi:10.3390/en11040724

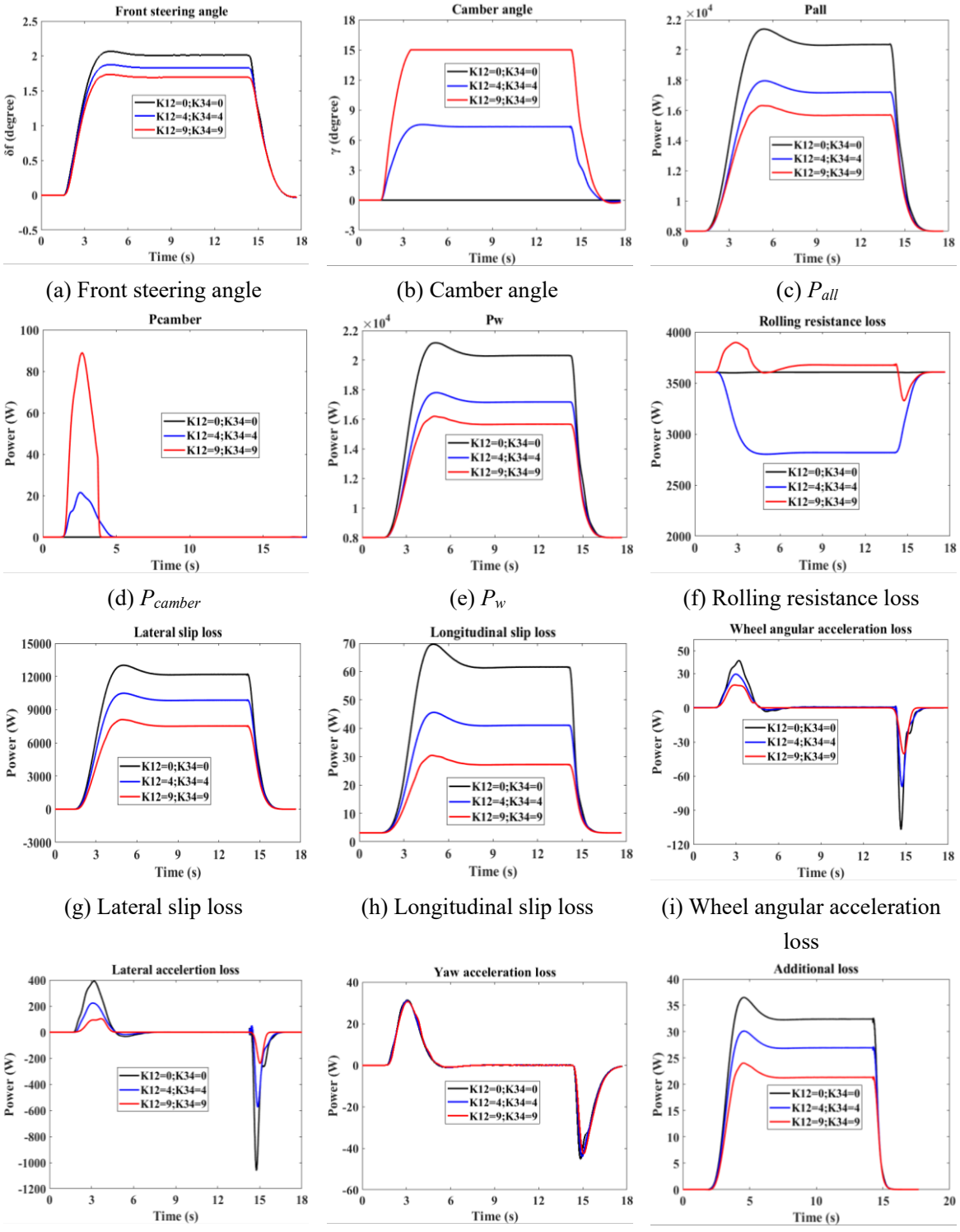

(a) Front steering angle (b) Camber angle (c) P_{all}

(d) P_{camber} (e) P_w (f) Rolling resistance loss

(g) Lateral slip loss (h) Longitudinal slip loss (i) Wheel angular acceleration loss

(j) Lateral acceleration loss (k) Yaw acceleration loss (l) P_a

Figure 11. Steering and camber angles as well as power losses at R=100 m and Vx=88.18 km/h.

From Figure 6(d), it is seen that camber angle can increase the aligning moment and this tyre property was also presented in [23]. The components of $M_{zi}\sin\gamma_i$ can have different influences on rolling resistance loss in different slip angle regions. From Figure 12, for R=100 m, V_x=62.3 km/h and a_y=3 m/s^2, the slip angles are comparatively small. Compared to K_{12}=K_{34}=4,

Preprints (www.preprints.org) | NOT PEER-REVIEWED | Posted: 9 February 2018 doi:10.20944/preprints201802.0078.v1

Peer-reviewed version available at Energies 2018, 11, 724; doi:10.3390/en11040724

the slip angles are further reduced by K_{12}=K_{34}=9 and then all aligning moments become positive, which increases the rolling resistance substantially and greatly weakens the camber's contribution to power reduction. However, from Figure 13, for R=100m, V_x=88.18 km/h and a_y=6 m/s^2 , the slip angles are seen to be comparatively large. Consequently, further increasing the camber angle, $\sum_{i=1}^{4} M_{zi} \sin \gamma_i$ does not increase much and the reduction of lateral slip loss still plays a dominant role in energy saving.

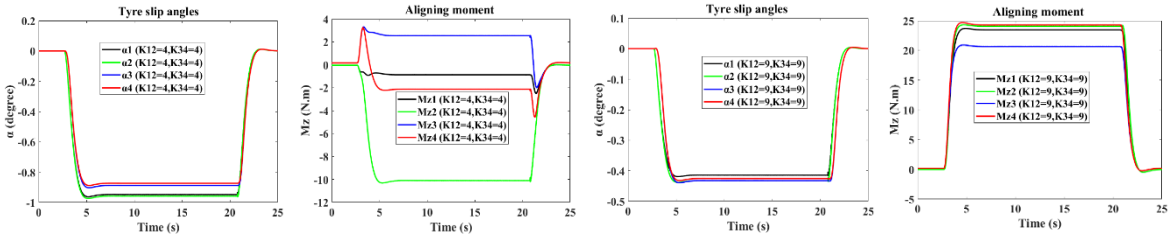

(a) α for K_{12}=K_{34}=4 (b) M_z for K_{12}=K_{34}=4 (c) α for K_{12}=K_{34}=9 (d) M_z for K_{12}=K_{34}=9

Figure12. Slip angle and aligning moment at R=100m and V_x=62.3km/h.

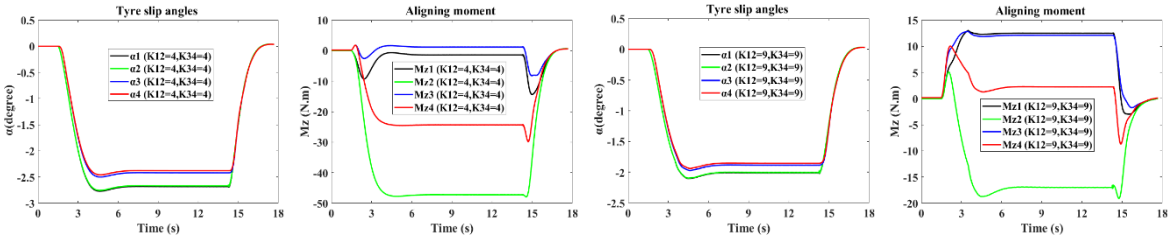

(a) α for K_{12}=K_{34}=4 (b) M_z for K_{12}=K_{34}=4 (c) α for K_{12}=K_{34}=9 (d) M_z for K_{12}=K_{34}=9

Figure 13. Slip angle and aligning moment at R=100 m and V_x=88.18 km/h.

5. Controller design for camber

Compared to the power loss without camber $P_{all}(0,0)$, the percentage of energy saving η with camber control can be described as

$$\eta = \frac{\int P_{all}(0,0)dt - \int P_{all}(K_{12}, K_{34})dt}{\int P_{all}(0,0)dt} \times 100\% \quad (22)$$

From Section 4, for R=100 m, V_x=62.3 km/h and a_y=3 m/s^2, when $K_{12} = K_{34} = 4$, the camber angles at steady-state cornering are found to be 6.5^0 and η is 8.31%; for R=100 m, V_x=88.18 km/h and a_y=6 m/s^2, when $K_{12} = K_{34} = 9$, the camber angles at steady-state cornering are 15^0 and η is 19.11%.

These results show that camber can be very promising to save energy during cornering. However, how to fully use the potential of camber for different driving scenarios remains to

Preprints (www.preprints.org) | NOT PEER-REVIEWED | Posted: 9 February 2018 doi:10.20944/preprints201802.0078.v1

Peer-reviewed version available at Energies 2018, 11, 724; doi:10.3390/en11040724

be explored and a camber controller needs to be designed. A more comprehensive test scheme has been developed and is shown in Table 3. Besides L=60 m and R=100 m, two groups of path parameters (L=30 m, R=50 m; L=90 m, R=150 m) are added. Six lateral accelerations (1, 2, 3, 4, 5 and 6 m/s^2) at steady-state cornering are studied and corresponding velocities are deducted.

Table 3. Path parameters, chosen velocities and lateral accelerations at steady-state.

R (m)	a_y (m/s^2)	V_x (km/h)	R (m)	a_y (m/s^2)	V_x (km/h)	R (m)	a_y (m/s^2)	V_x (km/h)
50	1	25.4	100	1	36	150	1	44
	2	36		2	50.9		2	62.35
	3	44		3	62.35		3	76.3
	4	50.9		4	72		4	88.1
	5	56.9		5	80.4		5	98.5
	6	62.35		6	88.1		6	108

Figures 14, 15 and 16 present the results for the simulation setups in Table 3 and the reference 0% energy saving planes are also plotted in these figures. Firstly, it is shown that the higher the lateral acceleration at steady-state cornering is, the more energy saving can be achieved. The main function of the camber control is to reduce the lateral slip loss and when the lateral acceleration is small during the cornering, the percentage of lateral slip loss of total power loss is small. Camber control therefore makes no significant contribution to energy saving. Because of different working slip regions of M_z introduced in Section 4.3, at low accelerations higher camber angle settings might increase rolling resistance loss considerably as can be seen from Figure 14 (a)(b)(c), Figure 15 (a)(b)(c) and Figure 16 (a)(b)(c). For 6 m/s^2, the results show that for larger values of K_{12} and K_{34}, more energy can be saved. But for the rest of the lateral accelerations there are maximum energy saving points. Above all, these points are not singular and many combinations of K_{12} and K_{34} can be chosen for energy saving control.

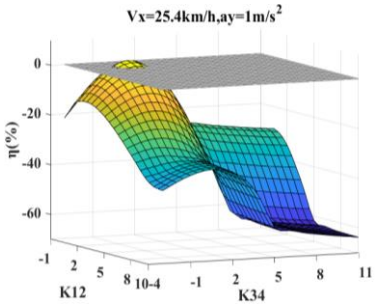

(a) V_x=25.4 km/h, a_y=1 m/s^2

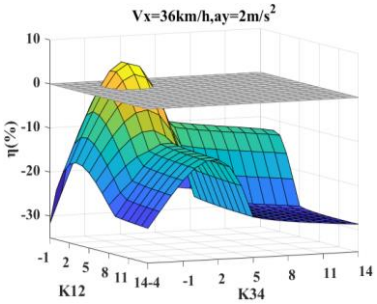

(b)V_x=36 km/h, a_y=2 m/s^2

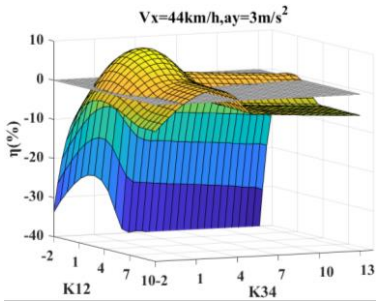

(c) V_x=44 km/h, a_y=3 m/s^2

Preprints (www.preprints.org) | NOT PEER-REVIEWED | Posted: 9 February 2018 doi:10.20944/preprints201802.0078.v1

Peer-reviewed version available at Energies 2018, 11, 724; doi:10.3390/en11040724

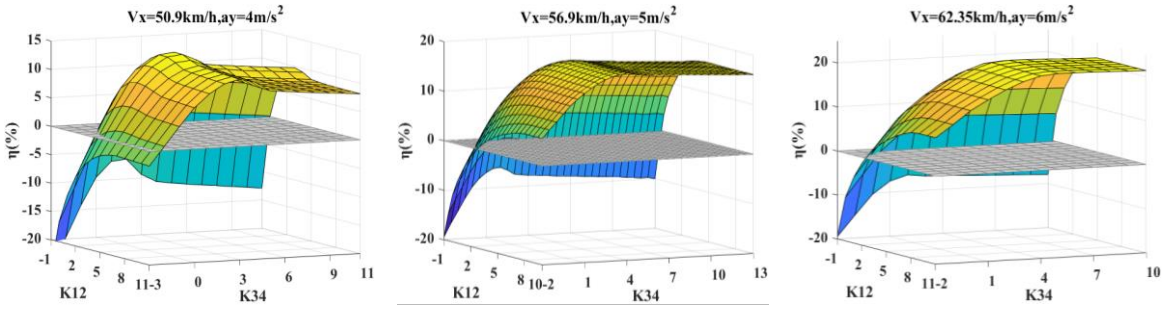

(d) V_x=50.9 km/h, a_y=4 m/s^2 (e) V_x=56.9 km/h, a_y=5 m/s^2 (f) V_x=62.35 km/h, a_y=6 m/s^2

Figure 14. Energy saving for different K_{12} and K_{34} for path R=50 m and L=30 m.

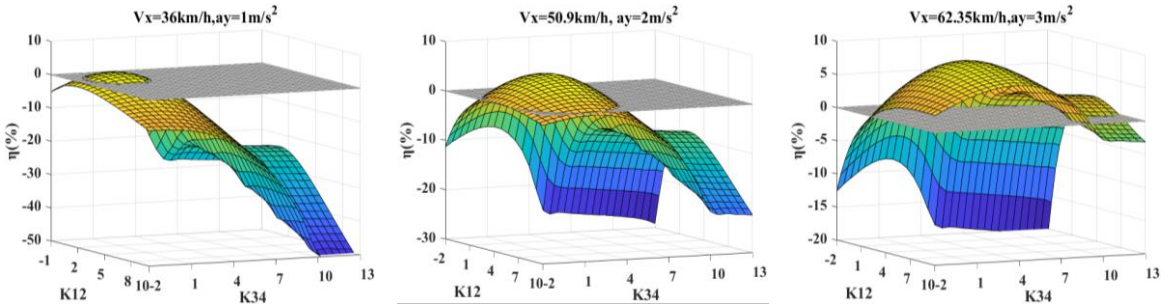

(a) V_x=36 km/h, a_y=1 m/s^2 (b)V_x=50.9 km/h, a_y=2 m/s^2 (c) V_x=62.35 km/h, a_y=3 m/s^2

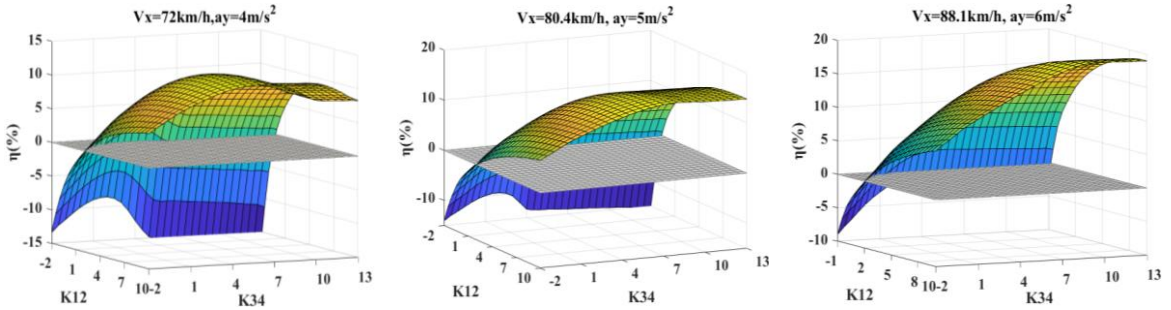

(d) V_x=72 km/h, a_y=4 m/s^2 (e) V_x=80.4 km/h, a_y=5 m/s^2 (f) V_x=88.1 km/h, a_y=6 m/s^2

Figure 15. Energy saving for different K_{12} and K_{34} for path R=100m and L=60m.

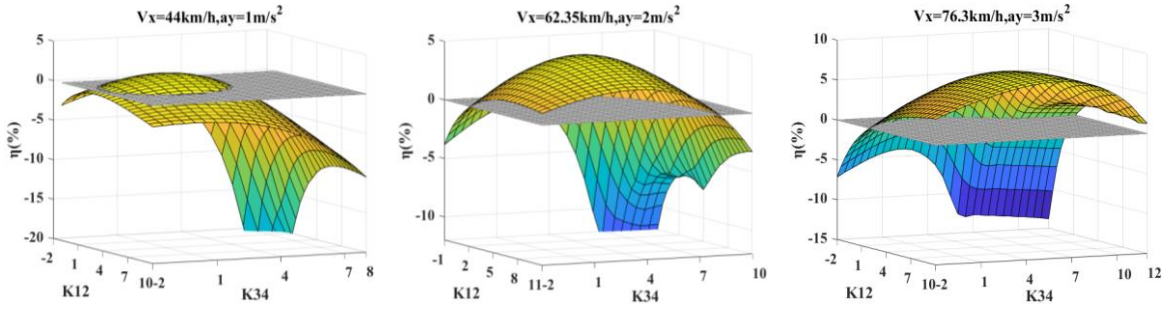

(a) V_x=44 km/h, a_y=1 m/s^2 (b) V_x=62.35 km/h, a_y=2 m/s^2 (c) V_x=76.3 km/h, a_y=3 m/s^2

Preprints (www.preprints.org) | NOT PEER-REVIEWED | Posted: 9 February 2018 doi:10.20944/preprints201802.0078.v1

Peer-reviewed version available at Energies 2018, 11, 724; doi:10.3390/en11040724

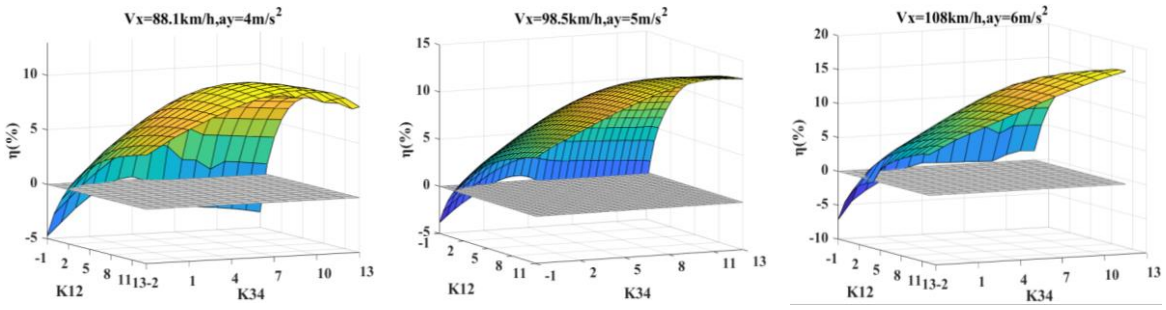

(d) V_x=88.1 km/h, a_y=4 m/s^2 (e) V_x=98.5 km/h, a_y=5 m/s^2 (f) V_x=108 km/h, a_y=6 m/s^2

Figure 16. Energy saving for different K_{12} and K_{34} for path R=150 m and L=90 m.

For the simplicity of the camber control, the same camber angles for the front and the rear tyres are preferred i.e., K_{12}=K_{34}. To study these assumptions, the combinations of K_{12} and K_{34} are chosen and the camber angles during the steady-state cornering part are also shown in Table 4. These combinations are the optimal points or near the optimal ones. It can be seen that for certain a_y during the steady-state cornering, the efficient camber angles are approximately equal.

As a consequence, it is assumed that the camber angle can be controlled with the information of a_y. A controller which uses a_y as criteria for the camber control is shown in Figure 17 and the mean value of the three camber angles in Table 4 for each lateral acceleration a_y is used. Although, at high lateral accelerations such as 6m/s^2 and above, camber setting larger than 15^0 may save more energy, the average driver generally drives below 4 m/s^2 and 6 m/s^2 or higher only occurs in extreme situations [24]. Also with the concern of suspension working space, 15^0 camber angle is still chosen for lateral acceleration higher than 6 m/s^2 in this work.

From Figure 10(a) and Figure 11(a), although implementing camber control can reduce steering angle, the reduction is small and the linear relation between δ_f and a_y for each constant velocity can be regarded to be unchanged. Therefore, a feedforward camber controller based on the information δ_f and V_x is designed for simulation purposes. With the designed camber controller, the percentages of energy saving for the chosen driving scenarios defined in Table 3 are shown in Figure 18. The results show that the designed camber controller has a very promising application prospect for energy saving.

Table 4. The chosen combinations of K_{12} and K_{34} in the study

a_y (m/s^2)	R (m)	V_x (km/h)	K_{12}= K_{34}	γ_1=γ_2=γ_3=γ_4 (degree)	η(%)
1	50	25.4	0.8	2.49	1.54
	100	36	1.5	2.35	1.49
	150	44	2	2.11	1.40
2	50	36	1.5	4.70	5.35
	100	50.9	3	4.77	4.70
	150	62.35	4	4.31	4.24
3	50	44	2	6.33	9.68
	100	62.35	4	6.47	8.31
	150	76.3	6	6.60	7.30
4	50	50.9	3	9.53	13.62
	100	72	6	9.78	10.75
	150	88.1	8.5	9.51	10.12

Preprints (www.preprints.org) | NOT PEER-REVIEWED | Posted: 9 February 2018 doi:10.20944/preprints201802.0078.v1

Peer-reviewed version available at Energies 2018, 11, 724; doi:10.3390/en11040724

	50	56.9	4.4	13.96	17.63
5	100	80.4	8.5	13.88	15.20
	150	98.5	12.5	13.98	13.31
	50	62.35	5	15.00	21.92
6	100	88.1	9	15.00	19.10
	150	108	13	15.00	16.89

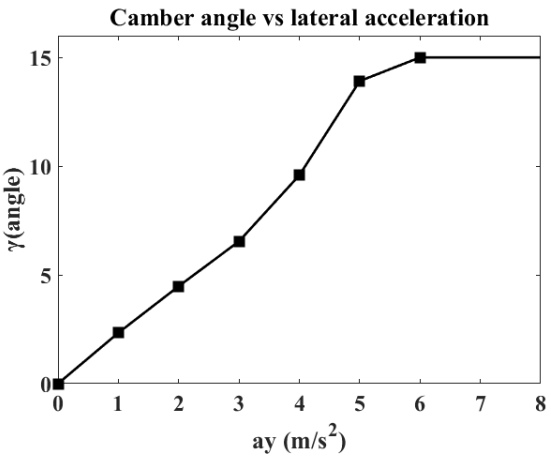

Figure 17. Camber control versus lateral acceleration a_y.

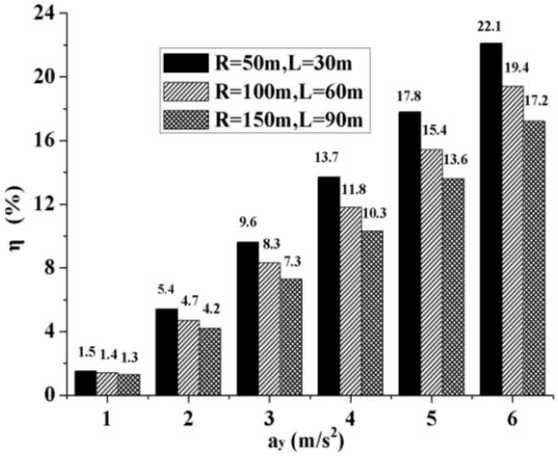

Figure 18. Energy saving for camber controller.

6. Conclusions

In order to analyse how a variation in camber angles influences the power loss during cornering, this paper formulates the components of the power loss. Different paths and velocities are designed for evaluation of camber effects. In Section 4.4, three combinations of K_{12} and K_{34}, two designed paths and two velocities are primarily studied. With camber control, the components of total power loss, which includes the power for controlling camber, are studied and from the results it is concluded that the three main components are aerodynamic loss, rolling resistance loss and lateral slip loss. For chosen combinations of K_{12} and K_{34}, camber control can reduce lateral slip loss but can also cause different changes in rolling resistance loss. In Section 5, different combinations of K_{12} and K_{34}, three paths and six velocities (corresponding to six accelerations at steady-state cornering) for each path are further studied.

The contribution of camber angle control to energy saving is obvious when lateral acceleration is high. There are multiple choices of K_{12} and K_{34} that can have a positive impact. The strategy of implementing the same camber angles for all tyres is chosen to be adopted. From Table 4, for each lateral acceleration the efficient camber angles are almost equal even if the velocities are different. The camber controller based on lateral acceleration is then developed and the effectiveness of the controller is evaluated. The results show that the proposed control algorithm is promising to save energy during cornering.

In future work, the longitudinal acceleration can be included and the tyre wear change due to camber control also needs to be considered. It is of great interest to explore expected energy saving within the probability density function of driving at various speeds and lateral accelerations with camber control. The change in the stability factors remains to be explored.

Preprints (www.preprints.org) | NOT PEER-REVIEWED | Posted: 9 February 2018 doi:10.20944/preprints201802.0078.v1

Peer-reviewed version available at Energies 2018, 11, 724; doi:10.3390/en11040724

Camber control is closely related to tyre properties and it is therefore important to know the tyre information before camber control is applied.

[Reference]

[1] Murata S. Innovation by in-wheel-motor drive unit. Vehicle System Dynamics, 2012, 50(6): 807-830.

[2] Wang R, Chen Y, Feng D, et al. Development and performance characterization of an electric ground vehicle with independently actuated in-wheel motors. Journal of Power Sources, 2011, 196(8): 3962-3971.

[3] Xiong L, Yu Z, Wang Y, et al. Vehicle dynamics control of four in-wheel motor drive electric vehicle using gain scheduling based on tyre cornering stiffness estimation. Vehicle System Dynamics, 2012, 50(6): 831-846.

[4] Kobayashi T, Katsuyama E, Sugiura H, et al. Direct yaw moment control and power consumption of in-wheel motor vehicle in steady-state turning. Vehicle System Dynamics, 2017, 55(1): 104-120.

[5] Kobayashi T, Sugiura H, Ono E, et al. Efficient direct yaw moment control of in-wheel motor vehicle, proceedings of AVEC 13th International Symposium on Advanced vehicle control, 2016.

[6] Chen Y, Wang J. Energy-efficient control allocation with applications on planar motion control of electric ground vehicles, proceedings of ACC American Control Conference, 2011.

[7] Suzuki Y, Kano Y, Abe M. A study on tyre force distribution controls for full drive-by-wire electric vehicle. Vehicle System Dynamics, 2014, 52(sup1): 235-250.

[8] Zetterström S. Vehicle wheel suspension arrangement: U.S. Patent 6,386,553. 2002-5-14.

[9] Manipal, Karnataka. Control of vehicle yaw moment by varying the dynamic camber, proceeding of AVEC'12, 11th international symposium on advanced vehicle control, 2012.

[10] Yutaka Hirano. Integrated control of tire steering angle, camber angle and driving/braking torque for individual in-wheel motor vehicle, proceeding of AVEC'12, 11th international symposium on advanced vehicle control, 2012.

[11] Jerrelind J, Edrén J, Li S, et al. Exploring active camber to enhance vehicle performance and safety proceeding of 23rd International Symposium on Dynamics of Vehicles on Roads and Tracks, Qingdao, China. 2013.

[12] Davari M. M., Jonasson M, Jerrelind J, et al. Rolling loss analysis of combined camber and slip angle control, proceedings of AVEC'16, 13th Symposium on Advanced Vehicle Control. 2016.

[13] Svendenius J, Gäfvert M. A brush-model based semi-empirical tire-model for combined slips. SAE Technical Paper, 2004.

[14] Svendenius J, Gäfvert M, Bruzelius F, et al. Experimental validation of the brush tire model. Tire Science and Technology, 2009, 37(2): 122-137.

[15] Pacejka H. Tyre and vehicle dynamics. Elsevier, 2004.

[16] Genta G. Motor vehicle dynamics: Modeling and simulation. World Scientific, 1997.

[17] Jazar R N. Vehicle dynamics: Theory and application. Springer Science & Business Media, 2013.

[18] Abe M. Vehicle handling dynamics: theory and application. Butterworth-Heinemann, 2015.

[19] Sharp R S, Casanova D, Symonds P. A mathematical model for driver steering control, with design, tuning and performance results. Vehicle System Dynamics, 2000, 33(5): 289-326.

[20] Winkler N, Drugge L, Trigell A S, et al. Coupling aerodynamics to vehicle dynamics in transient crosswinds including a driver model. Computers & Fluids, 2016, 138: 26-34.

[21] Wanner D, Drugge L, Edrén J, et al. Modelling and experimental evaluation of driver behaviour

Preprints (www.preprints.org) | NOT PEER-REVIEWED | Posted: 9 February 2018 doi:10.20944/preprints201802.0078.v1

Peer-reviewed version available at Energies 2018, 11, 724; doi:10.3390/en11040724

during single wheel hub motor failures, proceeding of FASTzero'15 International Symposium on Future Active Safety Technology Towards zero traffic accidents, 2015.

[22] Davari M. M., Jerrelind J., Stensson Trigell A., et al. Extended brush tyre model to study rolling loss in vehicle dynamics simulations. International Journal of Vehicle Design 2017, 73(4): 255-280.

[23] Fujioka T., Goda K. Tyre cornering properties at large camber angles: mechanism of the moment around the vertical axis. JSAE Review, 1995, 16(3): 257-261.

[24] Bosch, R. Automotive Handbook.2011.